

Fluorine-free transparent superhydrophobic nanocomposite coatings from mesoporous silica

Norbert J. Janowicz^{a,b}, Hangtong Li^b, Frances L. Heale^b, Ivan P. Parkin^b, Ioannis Papakonstantinou^c, Manish K. Tiwari^{a,d}, Claire J. Carmalt^{b*}*

^a Nanoengineered Systems Laboratory, Mechanical Engineering, University College London, London, WC1E 7JE, United Kingdom. Email: m.tiwari@ucl.ac.uk

^b Department of Chemistry, University College London, London, 20 Gordon Street, United Kingdom, WC1H 0AJ. E-mail: c.j.carmalt@ucl.ac.uk

^c Photonic Innovations Lab, Electronic and Electrical Engineering, University College London, London, United Kingdom, WC1E 7JE

^d Wellcome/EPSRC Centre for Interventional and Surgical Sciences, University College London, London, W1W 7TS, UK

KEYWORDS Superhydrophobic; Fluorine-free; Spin Coating; AACVD; Mesoporous Silica; PDMS; Metal Oxide crosslinking, Nanocomposite

Abstract

In recent decades, there has been a growing interest in the development of functional, fluorine-free superhydrophobic surfaces with improved adhesion for better applicability into real-world problems. Here we compare two different methods, spin coating and aerosol assisted chemical vapor deposition (AACVD), for the synthesis of transparent fluorine-free superhydrophobic coatings. The material was made from a nanocomposite of (3-aminopropyl)triethoxysilane (APTES) functional mesoporous silica nanoparticles and titanium crosslinked polydimethylsiloxane with particle concentrations between 9 wt% to 50 wt%. The silane that was used to lower the surface energy consisted of a long hydrocarbon chain without fluorine groups to reduce the environmental impact of the composite coating. Both spin coating and AACVD resulted in the formation of superhydrophobic surfaces with advancing contact angles up to 168° , a hysteresis of 3° and a transparency of 90% at 550 nm. AACVD has proven to produce more uniform coatings with concentrations as low as 9 wt% reaching superhydrophobicity. The metal oxide crosslinking improves the adhesion of the coating to the glass. Overall, AACVD was the more optimal method to prepare superhydrophobic coatings compared to spin coating due to higher contact angles, adhesion and scalability of the fabrication process.

Introduction

Superhydrophobic surfaces over recent years have been developed due to their applications in a range of areas, including self-cleaning surfaces,¹ reduction of drag,² anti-icing,^{3,4} self-healing⁵ and various other areas.⁶ For a surface to be superhydrophobic, the water contact angle needs to be $>150^\circ$ where the droplet can pin on the surface in Wenzel state⁷ or roll off the surface in Cassie-Baxter state.⁸ Self-cleaning, liquid mobility and drag reduction applications require Cassie-Baxter with non-uniform roughness. The droplet on such surfaces is mobile due to a phenomena called “contact angle hysteresis”.⁹ The physical basis of contact angle hysteresis (θ_Δ) is still unclear, however studies indicate that the phenomenon occurs due to non-ideal properties of real surfaces resulting in several metastable states or thermodynamically stable contact angles.^{10,11}

To fabricate superhydrophobic materials, fluorinated silanes or other fluorine based materials have been used and are widely reported in literature.^{12–15} Stable fluorinated groups decrease the van der Waal’s potential with the resulting electrostatic interactions limiting contact between the solid and liquid phases resulting in higher contact angles.¹⁶ In recent years, however, there have been many studies conducted on the environmental and health impacts of fluorinated compounds including fluorinated silanes.^{17–21} This has led to research into alternative methods for reducing the surface energy in order to achieve contact angles $>150^\circ$.^{1,5,22,23} Fluorinated silanes can be easily substituted with long chain hydrocarbon groups,^{24,25} as these inhibit water-solid interactions. However, greener alternatives rely solely on the van der Waal’s potential created by the hydrocarbon chain interactions which limit their effectiveness.

Inclusion of nanoparticles is a well-established approach to achieve morphology control and superhydrophobicity.^{26,27} Whilst there have been several studies on the control of particle morphology and size in synthesis, this paper focuses on the use of mesoporous particles with the aim of reducing particle density and increasing hierarchical roughness. The Stöber reaction and sol-gel process are still the main synthetic routes with many examples and reviews reported,^{28–30} including modifications that have shown the rise of various particle structures including the use of surfactants and templates to dictate the porosity and inner structure,^{31,32} and organic solvents for morphology modification.³¹ This paper bases synthesis on a previously reported method,³¹ for ex situ morphology control for aerosol assisted chemical vapour deposition and spin coating. One of the many challenges of working with nanoparticles is agglomeration, which this paper addresses through silanization to increase steric hindrance and reduce surface energy. Silica particles have been previously utilized in the fabrication of superhydrophobic coatings with a vast array of approaches.^{33–39} However, studies show that the addition of this inorganic filler to polymers to form nanocomposites often results in loss of transparency due to increased scattering. Alternative particle structures have been utilized to overcome this such as hollow, dendritic and mesoporous particles. Works by done on understanding the effect of the particle concentration such as by Vo et al,⁴⁰ demonstrate that particles with porous morphology reduce the impact on transparency of the coatings as the pores allow for the polymer to penetrate the particle. They also reported that lower concentrations also improve transparency.⁴⁰

Polydimethylsiloxane (PDMS) has often been used as the polymer of choice for superhydrophobic coatings^{41–44} because of its hydrophobic nature as well as

transparency when cured even at large thicknesses due to homogenous nature of the polymer. However, due to the minimal interacting sites the polymer has poor adhesive properties to glass, often requiring additional treatment of glass with plasma or chemical activation to increase hydroxylation. Some of these treatments can be hazardous as well as temporary once exposed to atmospheric conditions.

To address this concern, an *in situ* sol-gel approach to bridge PDMS monomers with metal oxides was adopted in this work.^{45,46} Metal alkoxides, such as titanium tetra(isopropoxide) [Ti(OⁱPr)₄] (TTIP), can be used to form titanium oxide linkages within the polymer network without impacting on its stability due to the low concentration within the system.⁴⁷ Furthermore, the adhesion between the hybrid polymer and glass substrate is enhanced due to the hydrolysis reaction between the transition metal (titanium) and free oxide species on the glass forming irreversible Ti-O-Si bonding.

Over the decades of development of liquid repelling surfaces, there has been several techniques developed and optimized for this purpose,^{6,48} which have been briefly outlined in Table S1. The main techniques described in this paper are spin coating^{15,49,50} and aerosol assisted chemical vapor deposition (AACVD),^{51–55} which are illustrated in Figure 1.

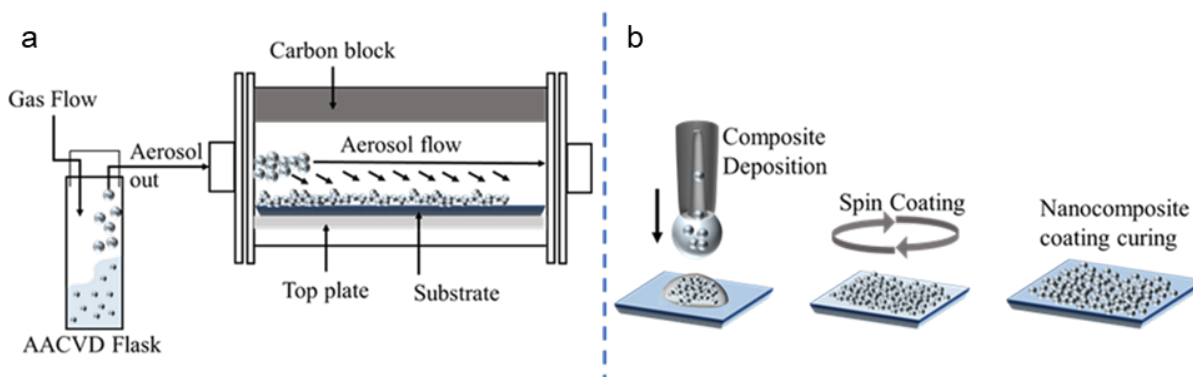


Figure 1. Schematic illustrations of our (a) AACVD and (b) spin coating procedures.

Both techniques allow for the nanocomposite to be directly deposited onto a substrate without modification to the solvent or polymer used. Furthermore, these methods could be scalable towards mass production of coatings but are different enough to yield variations in chemical and physical properties of the resulting nanocomposite coating.

This paper builds on the greener fluorine-free approaches whilst evaluating the effect that polymer crosslinking and manufacture techniques have on the resulting surfaces. It has been established that due to the non-polar chemistry of PDMS, the contact angle on a smooth block is $\sim 120^\circ$.⁵⁶ For the nanocomposite, PDMS was crosslinked with a titanium source in the form of TTIP and compared against a manufacturer supplied crosslinker. Unlike previous attempts, this work demonstrates that metal alkoxide in the presence of carboxylic acid is capable of crosslinking PDMS with successful curing and increased adhesion to the glass substrates while maintaining high degree of hydrophobicity in combination with AACVD.

The resulting coatings from both methods show a high degree of transparency whilst the non-toxic approach is easily scalable in the case of AACVD with significant reduction in particle loading concentrations with superhydrophobic behavior as low as 9 wt% compared to 41 wt% for spin coating. Furthermore, the resulting surface morphology demonstrates nano-micro hierarchal roughness for enhanced superhydrophobic behavior, which was further enhanced with fluorine-free hydrocarbon silanes. The methods were evaluated based upon chemical, physical and application properties. This was done through evaluation of morphology and bonding environments, adhesion, transparency, particle concentration required to reach superhydrophobicity and scalability potential. Overall, the paper presents a number of new findings. Firstly, the introduction of metal oxide crosslinking of PDMS has recently been gaining interest for the preparation of hybrid inorganic-organic polymer networks where the metal oxide provides additional properties to the coating such as the demonstrated enhanced adhesion of the nanocomposite to the substrate where the conditions in AACVD showed resulting adhesion resistance of up to 15 tape test cycles without highly impacting the transparency of the polymer. We are first report such improvement in hybrid inorganic-organic superhydrophobic PDMS nanocomposite. Second, the use of AACVD showed a large decrease in the required concentration of particles required for achieving superhydrophobicity (down to 9 wt% to polymer compared to 41wt% for spin coating) which is comparative to other coatings prepared by the method but without the need for fluorinated silanes. Third, the use of nanoparticles prepared ex situ demonstrated by this work, provides new opportunities to tailor the particle roughness at the nanoscale through highly controllable synthesis routes for the nanocomposite formation as well as

provides the opportunity to further functionalise the particles prior to coating to enhance surface functionality and enhance properties such as transparency and adhesion. Last but not the least, direct comparison of the spin coating and AACVD methods further demonstrates the advantages and limitations in fabrication of the coatings through using the same nanocomposite composition. Clearly, one might be more favoured over the other and demonstrating the overall potential of AACVD in manufacturing superhydrophobic coatings as a greener and more sustainable approach.

Results and Discussion

Mesoporous Silica Nanoparticles

A method presented elsewhere³¹, with the exclusion of dodecanol as depicted in Figure 2a-d, was followed using tetraethylorthosilica (TEOS) as precursor and cetrimonium bromide (CTAB) as morphology directing surfactant to obtain mesoporous 120 nm silica particles. Brief description is provided in the Experimental section. Each reaction step was indicated in the schematic with corresponding conditions from micelle formation and arrangement in Figure 2a, condensation of TEOS around the micelles in Figure 2b to the removal of the CTAB template using acidic alcohol wash in Figure 2c. Functionalization of the particles was achieved with (3-Aminopropyl)triethoxysilane (APTES) as indicated in Figure 2d to enhance the dispersion through the introduction of steric and functional hindrance as reported elsewhere.^{29,57}

Attenuated total reflectance Fourier-transform infrared spectroscopy (ATR-FTIR) characterization, shown in Figure 2e, was used to confirm successful washing and functionalization of the particles whilst nuclear magnetic resonance (NMR) in Figure 2f and scanning electron microscopy (SEM) in Figure 2g_i and Figure 2g_{ii} were used to

confirm particle size and silicon environments whilst TEM in Figure 2h was used to determine pore size. To evaluate the effect of mesopores on the coating, non-porous silica particles were synthesized with SEM images in Figure 2i confirming particle size.

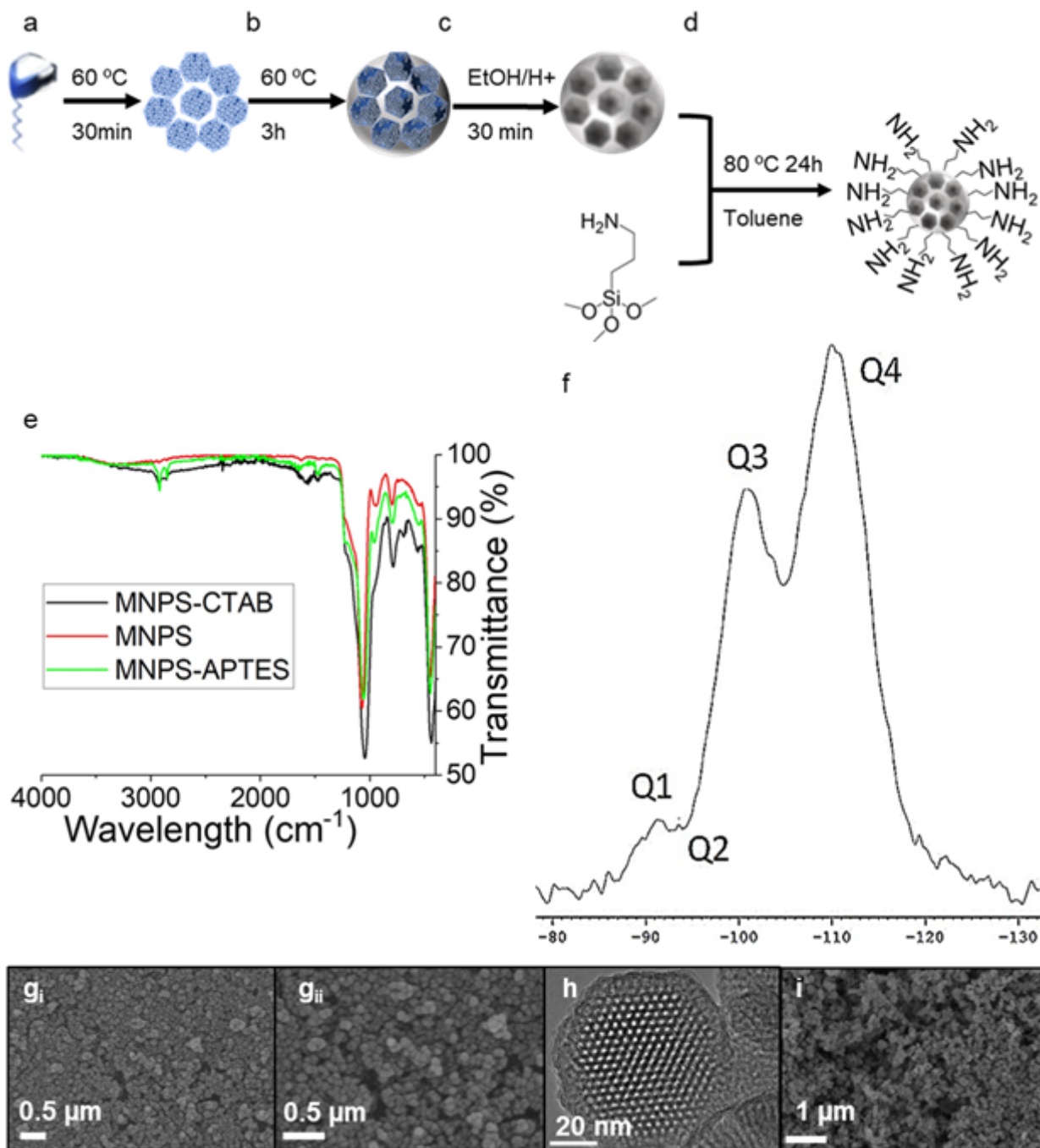


Figure 2. (a-d) Schematic of synthesis of mesoporous silica nanoparticles and APTES functionalization. (e) ATR-FTIR spectra of synthesis steps of mesoporous silica. (f) ^{29}Si NMR with labeled environments on silica particles (scale in chemical shifts in ppm). SEM images of synthesized mesoporous silica (g_i) before and (g_{ii}) after functionalization. (h) TEM of mesoporous silica. (i) SEM images of non-porous silica nanoparticles.

From the ATR-FTIR spectra (Figure 2e), the particles were confirmed to have fingerprint peaks for silica. Upon further study, red shifts in the spectra were observed, from 1086 to 1052 cm^{-1} (shift of 34 cm^{-1}) for transverse-optical mode of the Si–O–Si lattice and from 811 to 793 cm^{-1} (shift of 18 cm^{-1}) for Si–O–Si symmetric stretching vibration band. This indicates the formation of silica with a more open network (Si–O–Si bond) suggesting the presence of porosity in the sample.

The functionalization with APTES was also confirmed via ATR-FTIR, as shown in Figure 2e, with the presence of C–H stretch at 2900 cm^{-1} , as well as two small peaks 3240 cm^{-1} and 3360 cm^{-1} representing N–H stretch. Further peaks at 1610 cm^{-1} and 1300 cm^{-1} corresponding to C=N and C–N bonding can also be observed. The emergence of a peak $\sim 720 \text{ cm}^{-1}$, corresponding to SiOC interactions, can also be seen in the spectra.

To evaluate the silica environments present in the mesoporous silica nanocomposite, ^{29}Si -ssNMR was used, as shown in Figure 2f. Four distinct environments were observed, which contrasts with non-porous silica, where typically only one peak is observed in the ^{29}Si -ssNMR spectra since all the silicon atoms are present in one type of environment. However, when mesopores are introduced into the material, the number of binding

oxygen atoms to a silicon changes depending on the location of the binding in relation to the pore. Surface silica exists as quadruple bonded silicon to four oxygen atoms as shown at -110 ppm (Q4 in Figure 2f) which is associated to any silica complex, for example the same peak can be seen when analyzing sand.⁵⁸ Further peaks labelled as Q3 to Q1 in Figure 2f were observed, which are expected for mesoporous silica, providing evidence for the formation of the silica nanocomposite.⁵⁹

From SEM images in Figure 2g_i and Figure 2g_{ii}, an average particle size of 120 ± 5 nm was confirmed. This corresponded well to a size of 90-140 nm measured using dynamic light scattering (DLS) with highest intensity peak seen at 118 nm. Furthermore, the particles can be seen to be spherical shaped, which was reported by Han *et. al.*,³¹ indicating successful synthesis of the silica nanoparticles. Non-porous silica nanoparticles in Figure 2i demonstrated average particle size of 100 nm also. This was expected as the same synthesis procedure was followed with the exception of CTAB as no structure template was required.

Effect of mesoporosity on coating properties

Nanocomposite was formulated in one-pot approach depicted in Figure 3 and fully detailed in methodology section. In brief, a measured mass of APTES functional particles was mixed with PDMS to which titanium isopropoxide (TTIP) was added. The crosslinking of PDMS and TTIP was facilitated by acetic acid whilst the hydrophobic nature of the coating was boosted by the fluorine-free silane trimethoxy(octyldecyl)silane (TMODS) which worked to reduce surface energy of the surface.

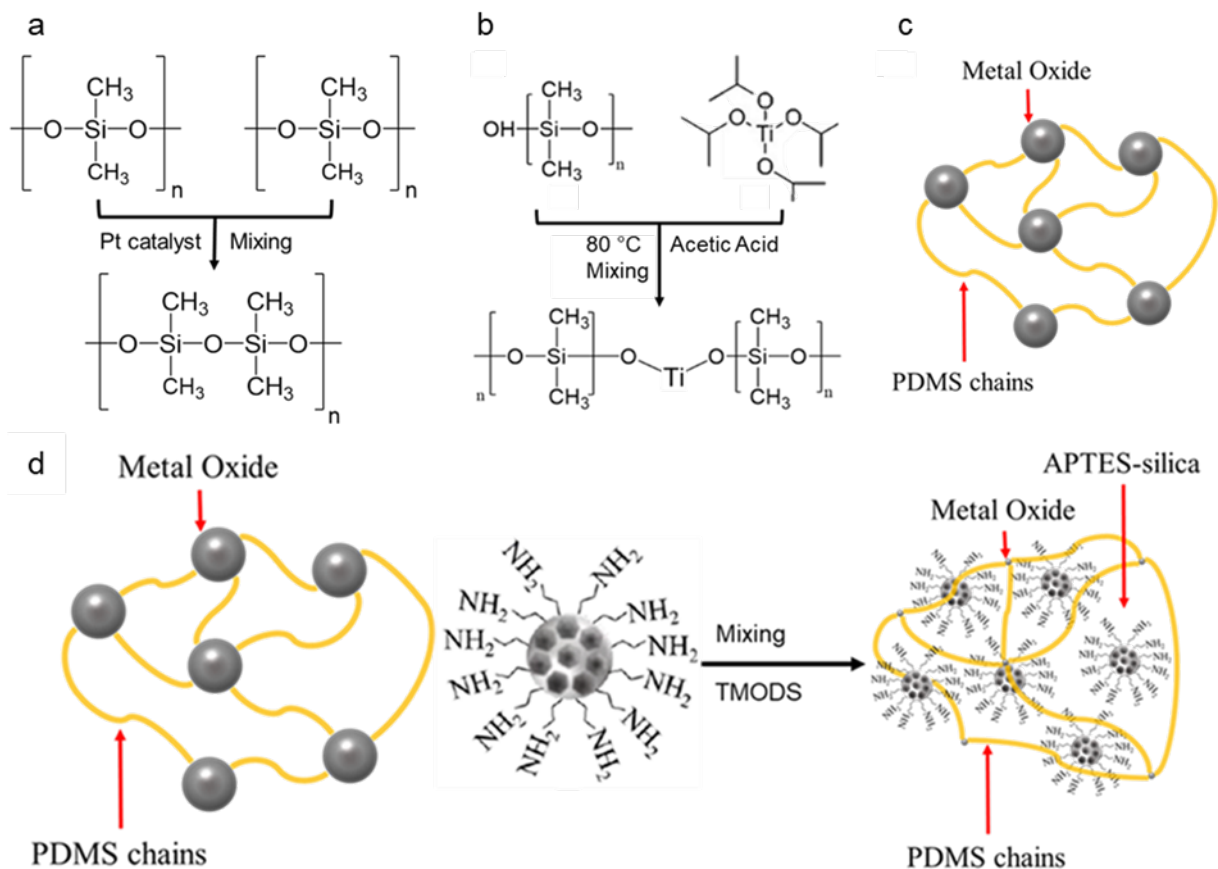


Figure 3. (a) Preparation of Sylgard 184 (b) Preparation of TiO-PDMS hybrid (c) diagram representation of the hybrid PDMS and (d) formation of the nanocomposite.

Mesopores permit the homogenizing of the particles within the polymer media in relation to achieving greater transparency to non-porous silica particles.⁶⁰⁻⁶² Functionalizing the silica particles with APTES groups works in two ways. Firstly, the grafting reduces the surface energy of the particles which promotes dispersion within organic solvent which is preferred by the polymer which improves the homogeneity of the coating improving transparency and adhesion. Secondly, the functionalization adds steric hinderance between particles by addition of larger functional groups reducing agglomeration of the particles in the composite as demonstrated by Figure 4.

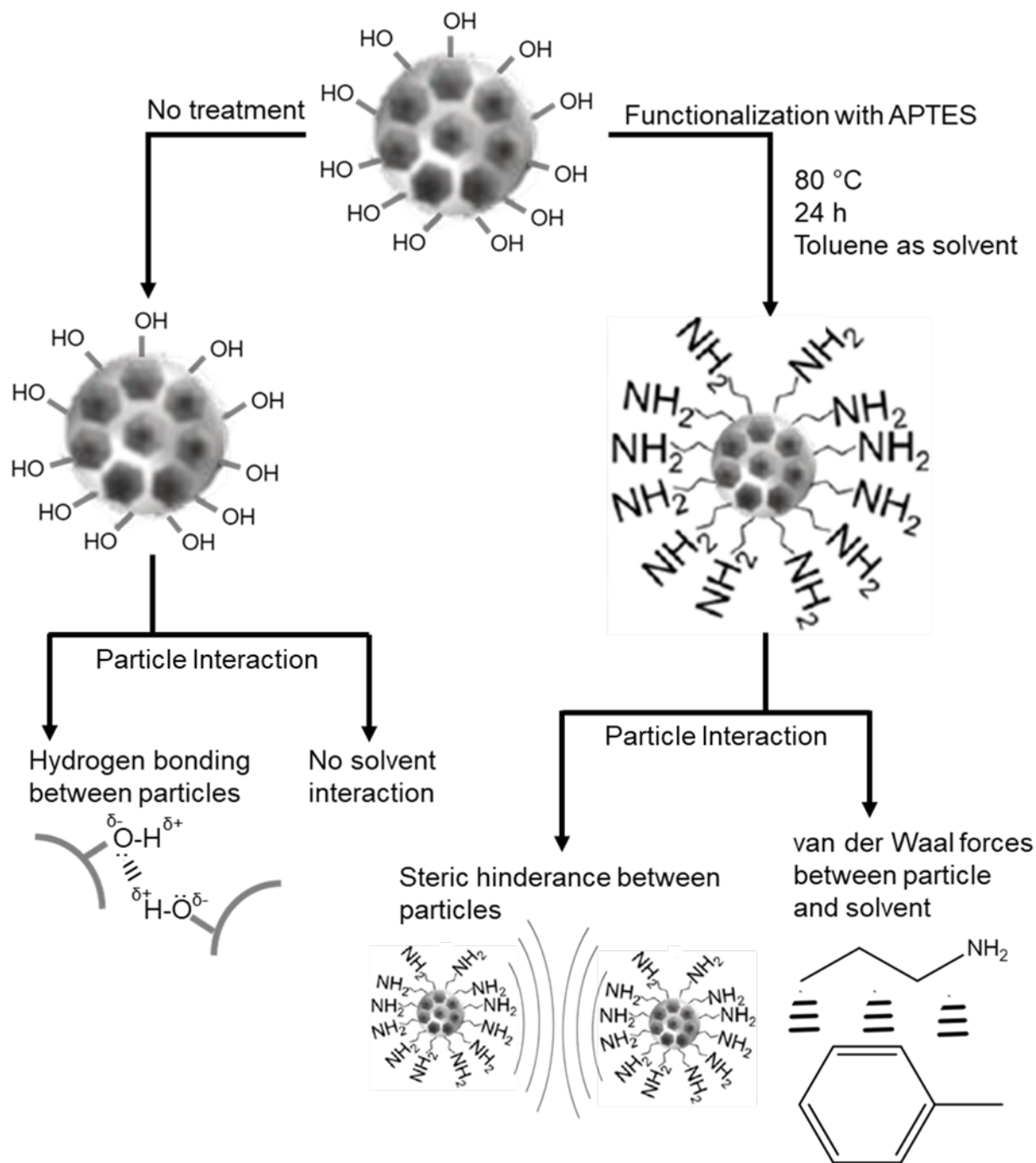


Figure 4. Visualization of the effect functionalization of the silica particle has on dispersion in solvent.

To examine whether mesoporosity influences the coating behavior, two samples (both at 43 wt% particle loading) were prepared by spin coating, one using non-porous 120 nm silica (Figure 2f-ii) and the other with mesoporous silica. Table shows the result.

Particle Type	Particle Conc. (wt%)	θ_A (°)	Transparency at 550 nm (%)
Mesoporous	43	152 ± 2	50.7
Non-porous	43	142 ± 6	47.5

Table 1. Evaluation of the effect of mesoporous silica on coating properties versus non-porous silica particles through contact angle and transparency.

From the comparison shown in Table , the effect of mesopores on the transparency of the resulting coating can clearly be seen, with enhanced transparency by 3.2%. This is supported by previous works in the literature which also noted the benefits of reducing the particle (mass) density in order to improve transparency of the coatings as the pores allowed for the polymer to fill the particles increasing homogeneity.⁶⁰ There is a 10° difference in the contact angles, which is due to the mesopores, as the coating was prepared using the same method. The surface exhibits non-uniform wetting behaviour with standard deviation being 6° for the average sample areas measured. The coating going from superhydrophobic to hydrophobic and the transparency reducing by 3.2% though the only change in particle structure is a clear indication of the benefits of using mesoporous particles with lower density and higher roughness over that of non-porous silica particles.

Spin coating

The deposition of thin films from a toluene solution of the APTES functionalised mesoporous silica and PDMS/Ti nanocomposite was conducted using a spin coater with 4,500 rpm for 60 seconds, the results of which are shown in Figure 5. The glass substrates were first allowed to reach the maximum acceleration before 1 mL of the solution was deposited onto the substrate. This was followed by 30 minutes curing (Figure S1). Samples prepared for additional annealing (Figure S2) were cooled to room temperature before being placed in an oven at 300 °C. The spin coated samples are abbreviated by SC in Figure 5. Table 2 below shows details of different samples (e.g. SC1A, SC1B, etc.). Sample SC3C was crosslinked using Sylgard crosslinker as comparison to metal oxide (TTIP). To evaluate the effect of temperature on the crystal structure of titanium species, a second batch of coatings was produced following same procedure with the addition of an annealing step where the coated samples were placed in an oven at 300°C for 60 minutes. The additional heating step was hypothesized to demonstrate similar behavior to that of AACVD method which is typically done at temperatures between 200-500 °C.

NAME	PARTICLE CONC. (WT%)	SECONDARY ANNEALING TEMP (°C)	Θ_A (°)
SC1A	33	-	142
SC1B	33	300	140

SC2A	41	-	152
SC2B	41	300	150
SC3A	50	-	154
SC3B	50	300	153
SC3C	50	-	155

Table 2. Experimental design of titanium crosslinked PDMS superhydrophobic coatings for Spin coating with indication of secondary heat treatment or not.

The surface morphology of the resulting coatings, as well as chemical composition, was analyzed using scanning electron microscopy Energy-dispersive X-ray spectroscopy (SEM-EDS) and ATR-FTIR, as shown in Figure 5. The SEM shows that a non-uniform roughness required for Cassie-Baxter state has been formed. However, the SEM image also shows that the resulting coating is non-homogenous where the particles agglomerate into micro dense and heavily charging microstructures, despite good dispersion prior to coating the glass substrates. For potential transparency, this limits the applicability of the method for this nanocomposite as such a high degree of roughness has been demonstrated to cause large scattering of light.⁶³

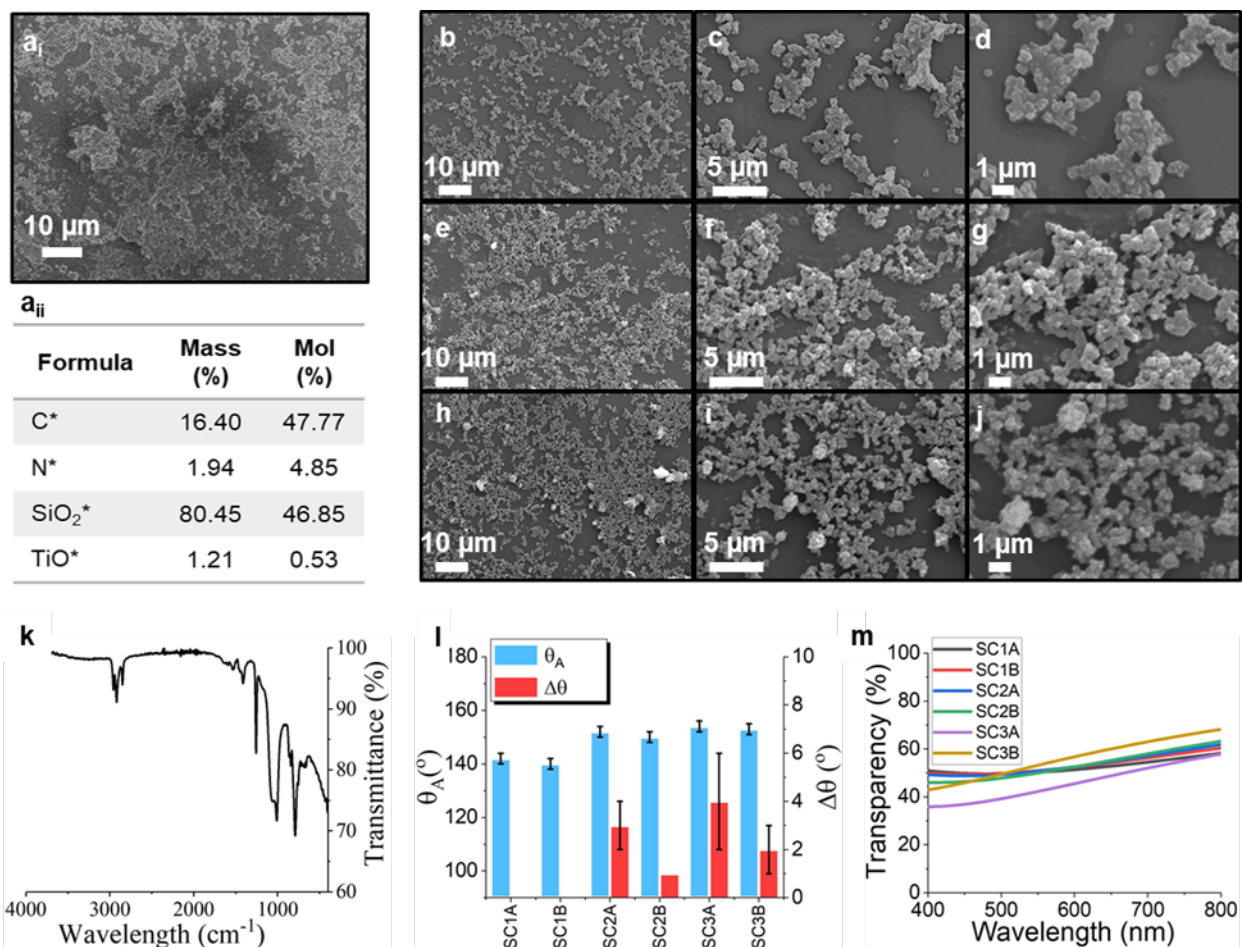


Figure 5. Morphology and chemical analysis of SC1A (a) SEM-EDS analysis with data in table. Evaluated zone shown in (a_i) and data in (a_{ii}). SEM images of spin coated samples (b-j) where (b-d) is SC1A (e-g) SC2A and (h-j) SC3A (k) ATR-FTIR of the coating. Functionality analysis of coatings (l) dynamic contact angle measurements showing advancing contact angle (θ_A) and hysteresis ($\Delta\theta$) (m) UV-Vis analysis of coatings with varying particle concentrations (wt%) and heat treatment.

The combined EDS and ATR-FTIR (Figure 5a) demonstrates that there was a successful incorporation of the titania species into the matrix with a calculated 1.93% of mass being

titanium. The FTIR spectra shows the presence of hydrocarbon groups (peaks around 2900 cm^{-1}) which are attributed to the silane (TMODS) used to lower the surface energy of the resulting material. Further peaks attributed to the particles can be seen around 1050 cm^{-1} and 790 cm^{-1} as described previously. However, the intensity of the peak at 790 cm^{-1} has increased compared to that of particles which is indicative of the Ti-O-Si bond formation. The peak at $\sim 420\text{ cm}^{-1}$ corresponds to Ti-O in amorphous titanium oxide species. This indicates that the coating process has not promoted formation of crystalline titania species, and as a result is not expected to have any photocatalytic properties similarly to what was reported by Dalod *et. al*,⁴⁵ Comparing Raman spectra of the spin coated samples before and after thermal annealing, as shown in Figure S3, limited difference in the peak intensities was observed with no additional peaks. This supports the data obtained from FTIR where no anatase peaks were noted.

This means that the thermal treatment after curing does not allow for the titanium (IV) oxide species to crystalize into photoactive species either in rutile or anatase and the morphology remains amorphous. From the data, clear peaks at 554 cm^{-1} , 789 cm^{-1} and 1093 cm^{-1} can be seen for amorphous silica along with peaks at 2413 cm^{-1} which combined are associated with silica nanoparticles and the polymer (PDMS) matrix. This was also observed in the EDS data as seen in Figure 5a.

The initial evaluation of the functionality of the fluorine-free coatings was conducted through morphology study (using SEM imaging at increasing magnifications, shown in Figure 5b-j for three different concentrations, c.f. Table 2) dynamic contact angle measurements and ultraviolet-visible spectroscopy (UV-Vis) as shown in Figure 5. The dynamic contact angles were measured to determine the state of wettability as well as

the degree of mobility of the droplet on the surfaces. The advancing and receding contact angles were recorded and processed using Matlab from which the difference between the two angles was calculated as the contact angle hysteresis.²⁶ Evaluation of the degree of transparency was done using UV-Vis.

The particle concentration greatly affects the wettability of the resulting coatings due to differences in the roughness. In Figure 5l, the concentrations shown are 33 wt%, 41 wt% and 50 wt%, the advancing contact angle reaches 140° for the lower concentration and increases to 154° for the 50 wt% (SC3A) sample. This indicates that the roughness created is too low for the lower 33 wt% and while the coating is hydrophobic the droplet is pinned to the surface and is unable to roll-off the material. The first sample to show superhydrophobic behavior is SC2A with advancing contact angle of 152° and hysteresis of 3°.

Further study of the effect of a second annealing step after curing shows that both θ_A and $\Delta\theta$ decrease afterwards which could be explained by the high temperature damaging the structure of the polymer matrix as seen by yellowing of the samples. However, this also increased surface uniformity as the PDMS was heated and the particles could possibly better set into the matrix.

This is further supported by the changes in transparency measurements where the coatings that have undergone thermal treatment exhibit higher levels of transparency. As shown in Figure 5m, the coatings SC3A and SC3B vary in transmittance by ~10% over the visible light region with average visible transmittance (AVT) of 46% for SC3A and 56% for SC3B; the secondary annealing improves transmittance for higher concentration but this is not seen at the lower concentrations. As indicated by SEM

imaging (Figure 5a and Figure 5b-j), the clusters formed on the surface due to particle agglomeration were less than a few microns in size. The transparency of these coatings does not seem to differ greatly by concentration of the particles. This indicates that at these concentrations the dispersion of particles needs to be further improved through functionalization to increase the steric hindrance between individual particles. Further functionalization in turn will diminish agglomeration resulting in less scattering and higher optical transparency.

Aerosol Assisted Chemical Vapor Deposition (AACVD)

Superhydrophobic coatings on glass substrates were deposited via AACVD from the precursor solutions with different concentrations of the APTES functionalized mesoporous silica and PDMS/Ti nanocomposite dissolved in toluene and with pure Sylgard (PDMS monomer) as additive to aid adhesion to the glass substrate, at temperatures between 200 and 400°C and 15-70 min deposition time. In this temperature range PDMS can survive short periods of time at high temperatures before it starts to break down whilst particle concentration is low to prevent large agglomeration and clogging of the equipment. Temperature, deposition time and particle concentration were varied to test their effect on surface morphology as well as optical transparency of the resulting material. The variables of each coating have been summarised in Table 3.

Name	PARTICLE CONC. (WT%)	TEMP. (°C)	DEPOSITION TIME (MIN)	Θ_A (°)
AD1A	23	300	70	157

Name	PARTICLE CONC. (WT%)	TEMP. (°C)	DEPOSITION TIME (MIN)	Θ_A (°)
AD2A	17	300	50	161
AD3A	9	300	50	162
AD1B	23	200	55	151 Wenzel
AD1C	23	400	60	164
AD1A15	23	300	15	168
AD1A20	23	300	20	161
AD1A30	23	300	30	167
AD1A50	23	300	50	160
AD1A60	23	300	60	162

Table 3. Experimental design of superhydrophobic coatings for AACVD method where AD = AACVD, 1-3 refers to concentrations and A-C indicates temperature.

Surface morphology and chemical composition of the AACVD coated samples were analyzed using SEM-EDS, X-ray photoelectron spectroscopy (XPS) and ATR-FTIR (Figure 6). From the morphology (Figure 6a and Figure 6b), there is clear indication of hierarchical roughness which facilitates Cassie-Baxter state. The EDS map shows consistent coverage of silica and titania where the latter seems to dictate the larger structures.

Despite playing a crucial role in the morphology of the coating, as expected, the concentration of Ti was low compared to that of Si or O (Figure 6c) which can be attributed to both the polymer and particles where these elements play a key role in structure. Carbon in the coating is of high prominence and this is the result of both polymer groups as well as the abundance of TMODS at the surface of the coating.

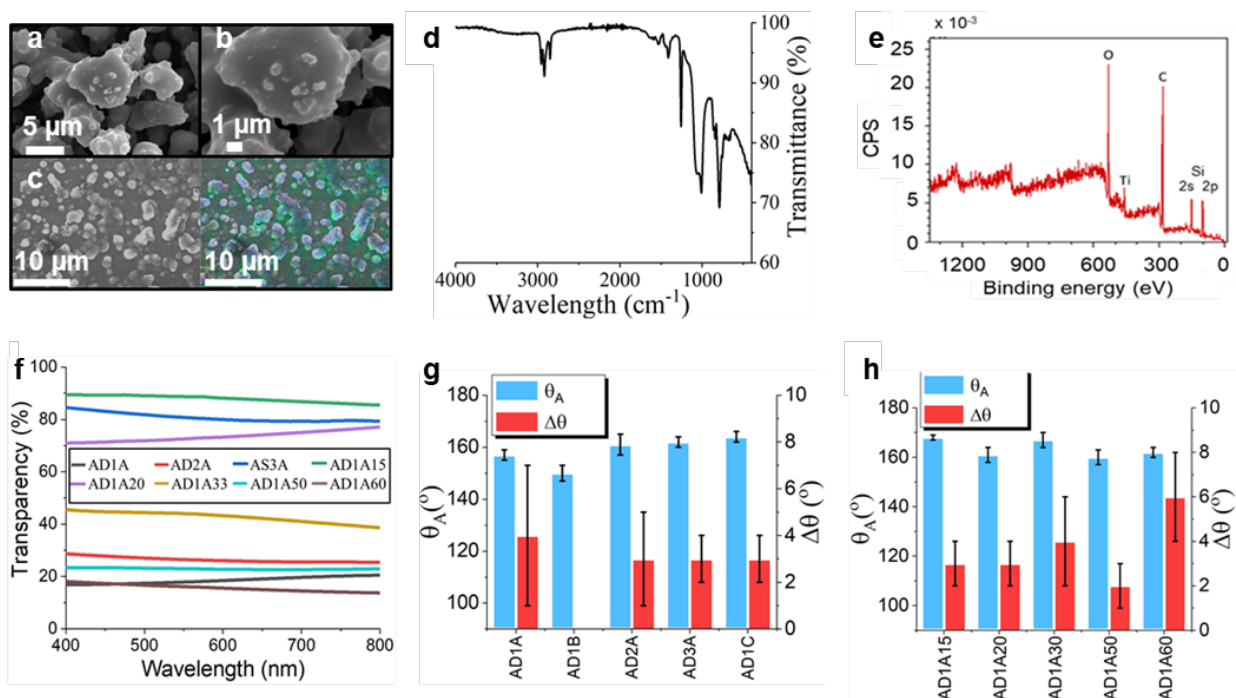


Figure 6. Morphology and chemical analysis of AACVD sample (a-b) SEM of AD3A (c) SEM-EDS analysis with composition map where Si - blue, Ti - yellow and O - pink. (d) ATR-FTIR of the coating (e) XPS survey spectra. Functionality analysis of coatings (f) UV-Vis analysis of coatings based on change in deposition time (AD1A15-60) and particle conc. (AD1-3A) (g-h) Advancing contact angle and hysteresis of samples with varying (g) temperature and particle concentration. and (h) deposition-time.

ATR-FTIR data was collected as shown in Figure 6d by scrapping the surface layers of the coating and analyzing the sample. Clearly defined peaks around 2900 cm^{-1} correspond to the C-H stretch from the silane functional group. Peaks corresponding to APTES can be seen in the analyzed sample, which indicates that the additional silane TMODES binds with the polymer rather than the particles. This is clear as there is not a strong catalyst added to the composite to cause amide bonding. Further peaks attributed to the particles were observed at $\sim 1050\text{ cm}^{-1}$ and 790 cm^{-1} as described in the spin coating section. In contrast to spin coated samples, there is a broadening and shift of the Ti-O peak around 420 cm^{-1} region and an emergence of a peak around 1600 cm^{-1} often seen in anatase. The data obtained from EDS is also supported by XPS (Figure 6e) indicating the presence of the four main elements: O, Ti, C and Si.

Evaluation of functionality of the fluorine-free coatings was conducted through UV-Vis spectra and dynamic contact angle measurements, as shown in Figure 6f-h. From the dynamic contact angle measurements, advancing (θ_A) and receding (θ_R) contact angles were recorded, with the difference between the two being the contact angle hysteresis ($\Delta\theta$).

To evaluate the effect of AACVD as a method on the transparency of the coating, UV-Vis (Figure 6f) was used. Focusing on the deposition times first, a clear correlation between deposition time and transparency in the visible region was demonstrated similarly to Tombesi *et. al.*⁶⁴ Their trend of decreasing transparency was due to increased time of each layer deposition. However, here the overall composite concentration changes with reduced time where sample AD1A15 was deposited for 15 minutes and exhibited transparency of $\sim 90\%$ compared to glass, whereas AD1A60

which was deposited for 60 minutes and only reached ~20% transparency. This indicates that with lower deposition time a more transparent coating can be achieved which relates to a lower concentration of the nanocomposite that coats the glass substrate, a trend supported in literature.⁶⁴

Comparing the effect of particle concentration on transparency, the decrease in particle concentration results in a higher degree of transparency from ~20% for 23 wt% to ~85% for 9 wt%. A similar effect can be seen by decreasing deposition time for the 23 wt% samples hence indicating a lower surface concentration of the particles on the final material. This can be explained by the fact that less coating reaches the surface as the deposition is not done to the completion of the nanocomposite. All samples made via AACVD achieved contact angles $>150^\circ$ (Figure 6g-h), however AD1B exhibited Wenzel state where the droplet pinned to the surface and no $\Delta\theta$ were measured, which could be the result of a lower temperature of 200 °C used for the deposition. This has been supported by literature where it was also noted that 200 °C was too low for the deposition of superhydrophobic surfaces with PDMS^{65,66}. The Cassie-Baxter coatings all exhibited $\Delta\theta$ below 10° indicating high droplet mobility, which are required for self-cleaning properties. Hysteresis values as low as $2^\circ \pm 1^\circ$ were also measured for some samples (see Figure 6h).

From varying the particle concentration, temperature and deposition time little difference to the contact angle or the $\Delta\theta$ was achieved providing the temperature was 300 °C or above. This contrasts with spin coating where a change in concentration dictated whether superhydrophobicity was achieved. Therefore, it was concluded that 300 °C was the optimal temperature and there was no advantage using higher temperature for

sample preparation in terms of contact angle, whilst concentrations as low as 9 wt% of particles was enough to reach superhydrophobicity. Despite minimal changes to the contact angle, there was a clear variation in scattering caused by the larger concentration of particles. This is supported by literature as higher concentration of particles means there is a greater chance of light being scattered by a particle.⁶³

Coating method comparison

Comparison of the two methods utilized for fabrication of the superhydrophobic surfaces revealed a range of characteristic differences. Focusing on the wetting behavior, composition data and morphology (Figure 7), films deposited via AACVD were superior compared to those from spin coating. Table below outlines the properties of the selected coatings for direct comparison of the two methods.

Name	Particle conc. (wt%)	Temp. (°C)	θ_A (°)
AD1A	23	300	157
SC3A	50	-	154
SC3B	50	300	153
SC3C	50	-	155

Table 4. Selection of coatings for comparison of the two methods based on highest concentration of particles for each method.

The morphology of samples prepared by the two approaches is compared in Figure 7a-l. The pillar-like structures seen in Figure 7a have been previously shown however,^{25,65,66} these were achieved through *in situ* sol-gel reactions within the deposition chamber

where here the same structures can be observed when *ex situ* synthesized particles are used. The deposition of the nanocomposite as an aerosol rather than relying on centrifugal forces to evenly distribute the particles has the benefit of further limiting the chance of particles agglomerating during the coating step with the same composite as seen in Figure 7d, Figure 7g and Figure 7j of the spin coated samples where the surface is covered by a polymer film with agglomerated particle sites.

AACVD prepared sample (AD1A) showed excellent self-cleaning properties (Figure 7p) as expected from its morphology and low contact angle hysteresis (Figure 7m and Figure 7o, replotted with data from Figure 5l, Figure 6g and Figure 6h). This was observed due to the prevalence of the surface energy reducing groups from the TMODS which have been bonded to the surface of the coating as indicated from ATR-FTIR analysis (Figure 5k and Figure 6d). The higher temperatures were not detrimental whilst the surface remained superhydrophobic and the removal of dirt did not weaken the effect.

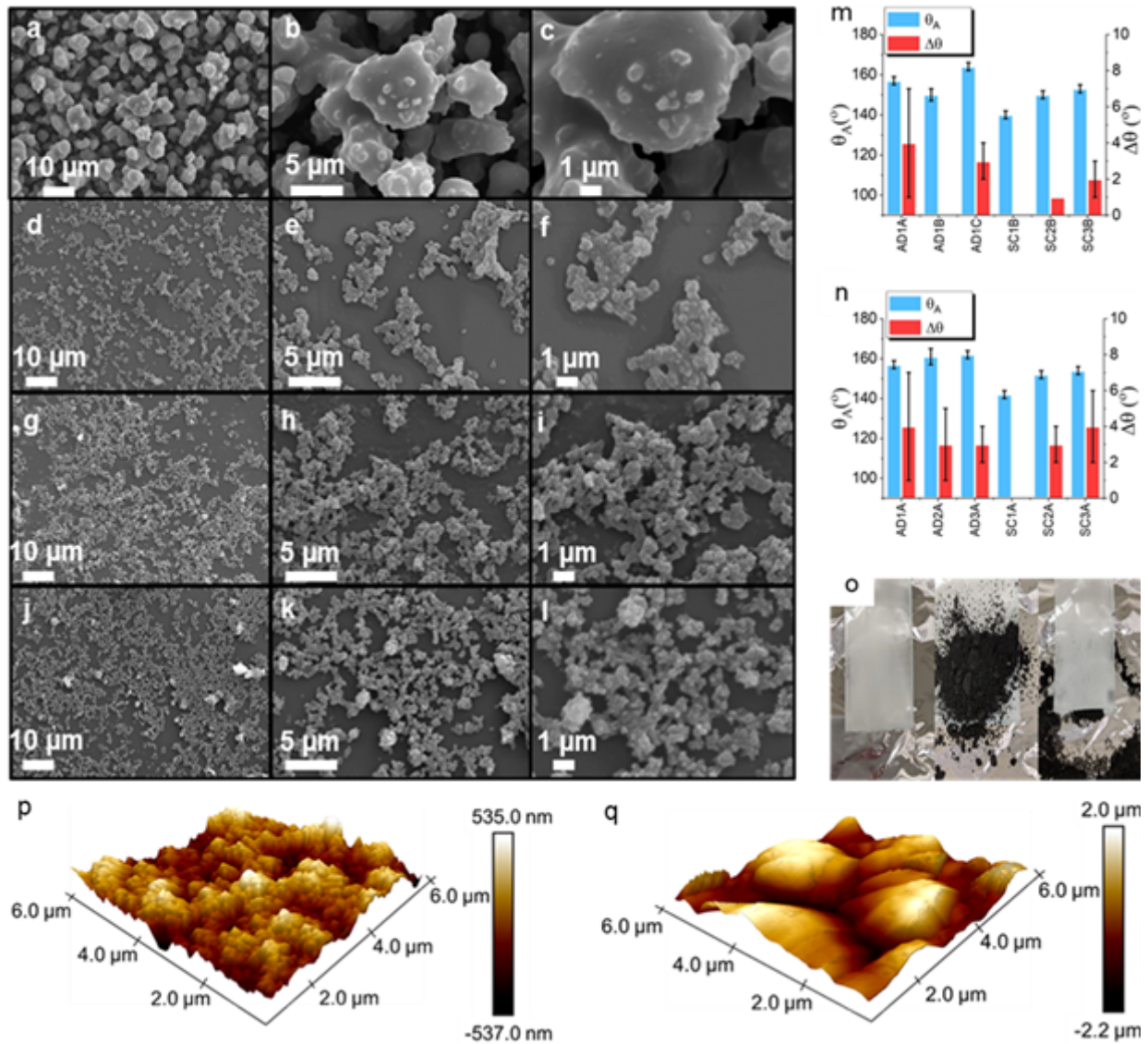


Figure 7. Morphology and wettability comparison. Comparative morphology of AACVD (a-c) AD1A and spin coated samples (d-f) is SC1A (g-i) SC2A and (j-l) SC3A. The same three magnifications were chosen with scales bar shown in images a-c. Influence of (m) particle concentration and (n) temperature on dynamic contact angles of coatings fabricated by both methods (o) self-cleaning of AD1A sample showing before, during and after cleaning. AFM study of (p) SC3A and (q) AD1A.

From the AFM data, there is a clear difference between the scale of roughness between the spin coated and the AACVD samples. The spin coated sample primarily remains at sub 500 nm roughness whilst the AACVD sample exhibits hierarchal roughness with micro and nano-sized features. The AFM data combined with SEM images provide clear view of the coating morphologies which explain for the difference in wetting behaviour and transparency. From the SEM it can be seen that the polymer is primarily responsible for the micro-structures which help to explain why the transparency of the coating is not adversely affected by the increased roughness compared to the spin coated samples as PDMS is transparent in Visible light range.

The hypothesis behind using TTIP was to introduce metal oxide pockets that would form stronger interactions between the substrate and the coating, hence enhancing the adhesion. This was tested through tape test as described in experimental section and analyzed using dynamic contact angle measurements as shown in Figure 8 due to loss of contact angle with the removal of the coating. To evaluate the effect of the metal oxide compared to standard crosslinker, the samples analyzed were compared to a coating prepared using standard crosslinker denoted SC3C (for spin coated samples) provided by Dowsil which was mixed at the recommended ratio of 10:1 polymer to bridging agent.

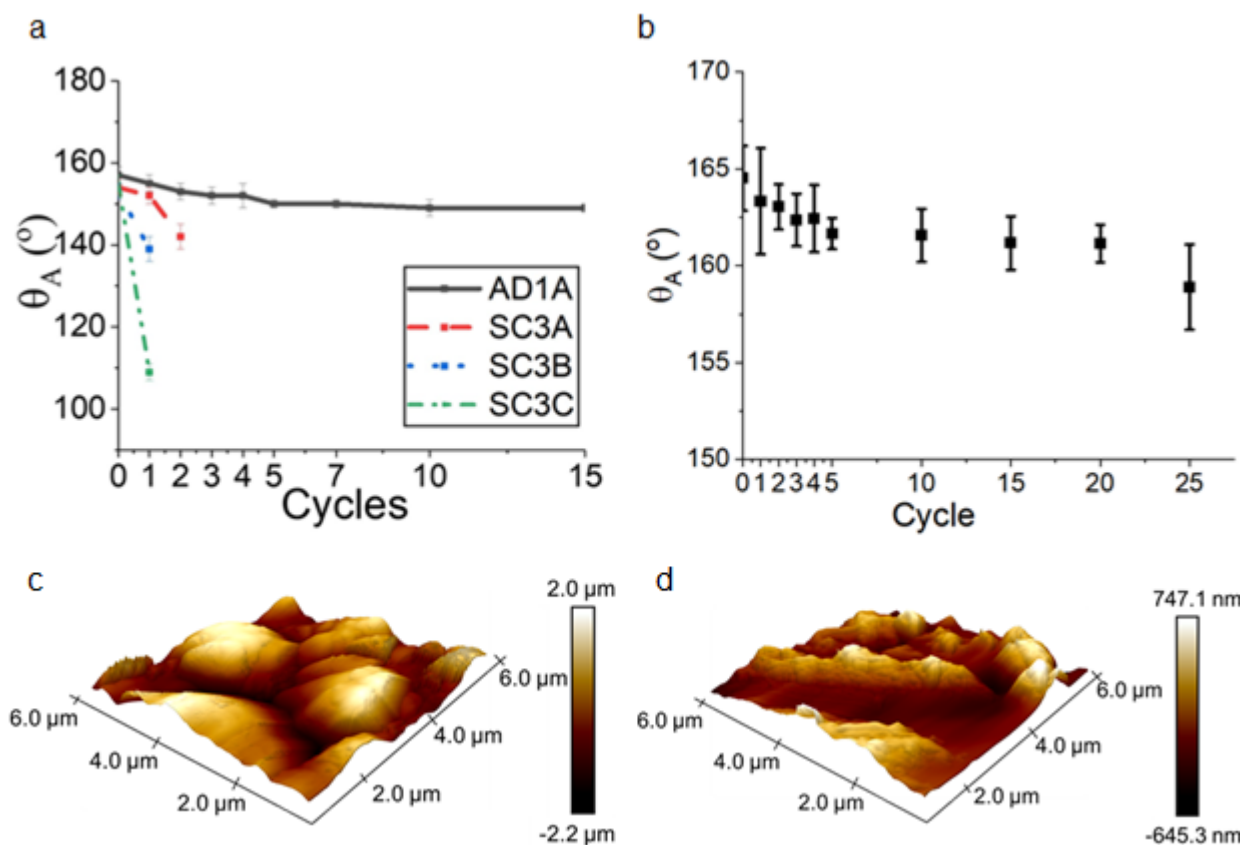


Figure 8. Cyclic tape peel test to assess substrate adhesion and durability of coatings. AACVD sample are stable well above 10 cycles. (b) Sandpaper abrasion test of AD1A showing durability above 25 linear abrasion cycles. AFM characterization of the surface of AD1A (c) before and (d) after the sandpaper test.

The test revealed that the standard crosslinker survived one peel cycle with a 40° decrease in contact angle whilst there was a large difference between spin coated samples and AACVD samples. The spin coated samples survived two and one peel cycle, respectively whilst the AACVD samples survived 15 peel cycles and still exhibited superhydrophobic behavior (Figure 8). It was apparent that, although the tape removed

a thin layer of the coating, the remaining coating remained superhydrophobic with an overall loss of 7° over the 15 peel cycles. This difference in adhesion is the result of the variation in fabrication method since in AACVD the substrate is heated prior to and during deposition whilst in spin coating the composite is heated post application to promote curing. In the hydrolysis reaction, heat treatment has been shown to favor the bonds in both gaseous oxygen and the oxygen bonded to the glass to break to free a binding site for the titanium to form O-Ti-O and Ti-O-Si bonds respectively.⁶⁷

The durability of the coating was tested through linear sandpaper abrasion cycles, as shown in Figure 8b, demonstrates the high resistance of the AACVD applied coating beyond 25 cycles. The coating displayed a total decrease in contact angle by 6° over the duration of the test whilst the droplet still rolled-off the sample indicating a retention of the Cassie-Baxter state. Comparatively, coatings in literature exhibit similar or weaker durability to the test such as the coating reported by Lu et al (40 cycles), Sebastian et al (20 cycles) or Wang et al (45 cycles) though it is worth noting the latter two tested longitudinally.⁶⁸⁻⁷⁰ Furthermore, despite the visible damage to the coatings' surface (Figure 8c-d), the high contact angle and Cassie-Baxter state remain which indicates in combination with the adhesion test that as a layer of the coating is removed, the one underneath is also superhydrophobic.

To visualize the differences between all the modified properties to the coatings a summative table (Table 5) was designed highlighting the key differences in physical and chemical properties of the coatings.

Sample	Particle conc. (%wt)	Transparent @ 550 nm (%)	Adhesion cycles
AD1A	23	20	15
SC3A	50	40	2
SC3B	50	55	1

Table 5. Summary comparison of the coatings based on particle concentration and durability tests and transparency.

Comparatively, coatings reported elsewhere achieve similar degrees of superhydrophobic behavior at much higher concentrations⁴² or required fluorination.^{2,12-}

¹⁵ Some examples have been summarized in Table 6 showing key variables.

Sample	Particle conc. (%wt)	Transparency (%)	θ_A (°)	Ref
AD1A15	9	90	168	This work
SC3B	50	55	153	This work
MPS-TEOS-POTS*	-	90	165	64
AACVD coated PTFE films*	-	91	169	71
Polyamide 12-SiO ₂ (1:4)	4	87	160	72
POTS- SiO ₂ *	100 (annealed particles)	-	163	73

Table 6. Comparison between manufactured coatings and literature based on particle concentration, transparency and advancing contact angle (θ_a). (*) indicates fluorinated components.

Both methods resulted in superhydrophobic coatings, however AACVD has demonstrated high contact angles ($168^\circ \pm 2$) and low hysteresis ($3^\circ \pm 1$) at very low particle loading concentrations- as low as 9 wt% (nanoparticle:polymer). Samples produced by AACVD typically achieved higher degrees of superhydrophobicity at lower wt% of particle to polymer, more uniform roughness and better definitions in PDMS intensities of the Raman spectra. All these factors as well as the tunability of the deposition times for the coatings results in higher transparency in the visible region and better adhesion (Figure 8) indicating better applicability of the coating.

Utilizing structured and porous silica has been shown by literature to great extent with success in transparency, durability and self-cleaning.^{33,37,39,74–80} Furthermore, the use of both non-fluorinated and fluorinated silanes along side of these has yielded in very good coatings with high contact angles and low hysteresis.³⁶ However, their application withing deposition systems has been limited due to difficulty of achieving homogenous dispersions in polymeric solutions which is why a large number of publications choose to utilize a sol-gel route where precursors are mixed with the polymer then deposited onto substrates where particle growth occurs at the surface of the material.^{80–83} The use of mesoporous particles synthesized *ex situ* permits to optimize the structure of the particle prior to coating deposition allowing for control in particle size, morphology and

functionality which the benefits can be seen from fabricated coatings. Furthermore, the presence of the pores has been shown to permit the polymer to fill them which resulted in higher transparency by further homogenizing the coating whilst the hierarchal structures gave greater contact angles at lower concentrations. From Table 6, AD1A15 shows competitive transparency and contact angle to those reported in literature despite not utilizing fluorinated silanes. This indicates that the synthesized coating is an environmentally friendlier alternative in achieving superhydrophobicity. Furthermore, the introduction of the titanium species provides stronger adhesion of the coating to the glass increasing durability to over 15 tape test cycles. The self-cleaning properties provide applicability within wall treatments, reducing water waste in cleaning surfaces from dust as well as prevent staining from water-based liquids. Reducing deposition times for the AD1A series has shown transparency of up to 90% in the visible region.

Conclusion

Successful synthesis of mesoporous silica nanoparticles has been demonstrated and characterized through solid-state NMR, FT-IR and SEM imaging. The functionalization of the particles was confirmed with peaks at 2900 cm^{-1} and two small peaks 3240 cm^{-1} and 3360 cm^{-1} representing N-H stretching vibrations. This in turn aided in the dispersion of the particles in the solvent used for the nanocomposite as well as creating additional sites for further silane and carboxylic acid interactions.

By dispersing the functionalized mesoporous silica in PDMS cross-linked with titania, derived in situ from titanium alkoxides precursors, a stable fluorine-free material system was formulated for synthesis of transparent superhydrophobic surfaces. Overall, a facile fabrication of fluorine-free superhydrophobic material with good adhesion to substrate

has been demonstrated through AACVD, with particle concentrations being as low as 9 wt%. Compared to spin coating, this method is highly scalable and requires much lower concentration of particles to achieve better results. The introduction of metal oxide (titania) species into polymer matrix enhanced the durability of the coating without diminishing desired properties with a clear indication of the formation of the desired Ti-O-Si bonds through ATR-FTIR indicative of metal oxide bonding to the glass substrate. Finally, the utilization of pre-synthesized mesoporous silica particles grants further control over surface nanoscale morphology with tunability of the size, shape and distribution of the mesopores ex situ to the coating process.

This work demonstrates the use of a nanocomposite in AACVD which allows for further functionality within the coating through utilization of varied particle and of different morphologies. The resulting transparent and fluorine-free coating (AD1A15), demonstrates potential applications in superhydrophobic windows and with further development and testing car windshields.

Experimental

Materials

Tetraethyl orthosilicate (TEOS), titanium isopropoxide (TTIP), cetyltrimonium bromide (CTAB), sodium hydroxide, hydrochloric acid, acetic acid, (3-Aminopropyl)triethoxysilane (APTES), trimethoxy(octadecyl)silane (TMODS), Sylgard 184 (PDMS) with curing agent (Dow, UK), Toluene, Ethanol. All chemicals were obtained from Merck unless indicated otherwise and used as obtained from supplier without any modifications.

Particle synthesis

To obtain mesoporous 120 nm silica particles, a method presented elsewhere³¹ was followed with the exclusion of dodecanol. In brief, 0.3 g of sodium hydroxide was dissolved in 500 mL of distilled water under fast magnetic stirring of ~1000 rpm. The basic solution was heated to 60 °C and 1 g of CTAB was added and slowly stirred until fully dissolved at a rate of 350 rpm. It took ~30 minutes for the surfactant to dissolve. Subsequently, 7.5 mL of TEOS was added dropwise over a 2 minutes period and the reaction was kept under increased speed of magnetic stirring (1000 rpm) for a further 3 hours. Upon completion of the reaction, the suspension was left to cool to room temperature and the particles were collected via centrifugation at 10,000 rpm for 15 minutes. The particles were washed with ethanol and re-dispersed in acidic alcohol (1 ml HCl in 100 mL ethanol) and stirred at room temperature for 30 min to remove the surfactant template from the mesopores. The sample was then once more collected and washed in ethanol before drying in an oven overnight at 80 °C.

Functionalization of the particles was achieved with APTES to enhance the dispersion through introduction of steric and functional hindrance. As reported elsewhere,⁸⁴ 1 g of particles was dispersed in 50 mL of toluene followed by the addition of 3 mL of APTES. The suspension was heated to 80 °C and stirred for 24 h. The resulting particles were centrifuged (10,000 rpm, 15 min) and washed with ethanol then dried at 80 °C overnight.

Nanocomposite synthesis

A one-pot approach for the preparation of the polymer-nanocomposite was designed to simplify the coating step.⁸⁵ Pre-determined concentration of APTES functionalized nanoparticles (in w/w% of nanoparticles: PDMS) was dispersed in 20 mL toluene, 0.3 g

acetic acid and 0.15 g TMODS with sonication for 60 minutes in cold water. The suspension was left to reach room temperature followed by the addition of 1 g of PDMS base agent and 0.8 mL TTIP. The colloidal suspension was stirred for 60 minutes to homogenize the coating. A comparison coating was produced with Sylgard 184 crosslinker instead of TTIP with a ratio of 1:10 (Crosslinker: PDMS) as advised by manufacturer.

Spin Coating

Glass substrates were coated with a 1 mL of suspension of the APTES functionalised mesoporous silica and PDMS/Ti nanocomposite in toluene at 4500 rpm for 60 seconds where the addition was done once the substrate reached maximum speed followed by curing on a hot plate at 200 °C for 30 minutes. The sample was left to cool and full characterization of surface morphology and wettability followed.

Aerosol Assisted Chemical Vapor Deposition (AACVD)

The APTES functionalised mesoporous silica and PDMS/Ti nanocomposite was also used for AACVD. The AACVD experiments involved depositions using a cold-walled horizontal-bed chemical vapour deposition (CVD) reactor described previously.^{53,55,64} For these depositions, the reactor was assembled such that the carbon heating block was positioned above a plate (145 mm x 45 mm x 4 mm) which supported the glass substrate 5 mm below and parallel to the carbon block. This resulted in a top-down heating configuration. This assembly was then enclosed within a quartz tube. Once the set reactor temperature (200, 300 or 400 °C) was reached, a PIFCO ultrasonic humidifier (power 25 W, frequency 40 kHz) was used to form a precursor aerosol from 20 mL of composite in toluene, which was transported to the heated substrate using nitrogen

carrier gas (1 L/min). Depositions were carried out for various durations (15-70 min) following which time the coated substrates were cooled under nitrogen and handled in air.

Characterization

Surface morphology of the samples was observed using SEM. Images were obtained using JEOL JSM-IT100. To prevent charging, samples were gold-sputtered with SC7620 mini sputter coater. The SEM images for morphologies of AACVD superhydrophobic coatings were generated under the JSM-7600F Field Emission SEM, JEOL, Japan. Vacuum sputtering samples with very thin gold film in order to improve the electrical conductivity of surface. The element analysis and distribution were carried out using energy-dispersive X-ray (EDS) Oxford instrument, the United Kingdom. Vacuum sputtering samples with very thin carbon film.

ATR-FTIR measurements were taken using MIRacle™ single reflection horizontal ATR accessory with a ZnSe single reflection crystal plate. The analysis was done in the range of 400 to 4000 cm^{-1} .

Solid-state NMR experiments were carried out on Bruker Avance 300 spectrometer with 7.05 T wide-bore magnet at ambient probe temperature. High-resolution solid-state ^{29}Si were recorded at 59.6 MHz using a standard Bruker 4 mm double-resonance magic-angle spinning (MAS) probe. Solid materials were packed into zirconia rotors of 4 mm external diameter and spun at the MAS frequency of 8 kHz with stability better than 3 Hz. High-resolution solid-state ^{29}Si NMR spectra were recorded using MAS and high-power proton decoupling. Typical acquisition conditions for ^{29}Si MAS experiments were: ^{29}Si 30° pulse duration = 1.8 μs ; recycle delay = 30 s; acquisition time = 43 ms. ^{29}Si

chemical shifts are given relative to tetramethylsilane (TMS). Tris(trimethylsilyl)silane (TTMSS) was used for the chemical shift calibration, with the ^{29}Si chemical shifts of -9.84 ppm and -135.4 ppm relative to TMS. X-ray photoelectron spectroscopy (XPS) was performed by Thermo theta probe spectrometer under the base pressure of 5×10^{-10} mbar using the monochromatic Al K- α photoelectron spectrometer with photon energy 1486.6 eV. Raman spectroscopy of the coatings was conducted using Renishaw InVia Raman microscope with a 532 nm laser. The samples were measured using sweep scan mode with 100% laser power and scanning time of 10 seconds repeated 5 times to improve the definition of the peaks.

X-ray photoelectron spectroscopy (XPS) was performed by Thermo theta probe spectrometer under the base pressure of 5×10^{-10} mbar using the monochromatic Al K- α photoelectron spectrometer with photon energy 1486.6 eV.

For quantitative analysis of coating wettability, advancing and receding contact angles were measured. Distilled water droplets were generated using a needle connected to a syringe pump. The pump was run in infusion and withdrawal modes to create advancing and receding contact angles, which were recorded using a CMOS camera connected to a Navitar zoom lens. The recordings were digitized into still images and the images were used to measure the advancing and receding contact angles with the help of a MATLAB based image processing script developed in house.²⁶

Ultraviolet-visible (UV-VIS) transmittance spectrum was recorded using two machines due to availability. The spin coated samples were recorded using a Shimadzu UV-1800 spectrophotometer double beam instrument over a wavelength range of 400–800 nm

whilst AACVD samples were recorded using a Shimadzu UV-2600 spectrophotometer single beam instrument over a wavelength range of 200–800 nm.

Adhesion tests

The adhesion was tested using tape-peeling test standard described by ASTM D3359-09^{ε2}. The coated side of the sample had an elcometer 99 adhesive tape adhered with the use of a 200g (2.25 KPa calculated pressure) block rolled over it twice and then the tape was peeled off. The effects were evaluated using contact angle measurements.

Abrasion tests

The durability of the coating was evaluated using linear abrasion cycles as reported elsewhere. In brief, the sample was placed on sandpaper (Standard glasspaper, Grit No. 240, G.C.P Silicon Carbide Waterproof Abrasive Paper Electro Coated from Sharpness) with a weight of 100 g and moved in a linear fashion longitudinally and transversely by 10 cm in each direction. This is what is defined as a cycle. The contact angle was taken and record after each cycle.

Self-cleaning tests

Self-cleaning applications were evaluated by dirtying the coating with graphene. The dirty sample was placed at an angle to facilitate directional droplet rolling and a video was recorded.

Supporting Information

The supplementary Information document contains following sections: Summary table of fabrication techniques; TGA analysis of mesoporous silica particles; Explanation of curing; Explanation of annealing; Raman analysis of the coatings.

Acknowledgment

The authors would like to acknowledge the technical support of Steve Firth for help with transmission electron microscopy and Abil Aliev for help with solid state ^{29}Si NMR. Furthermore we would like to thank Benjamin Bowles for the support with TGA analysis.

Funding

We acknowledge funding from EPSRC DTP for N.J.J. (Grant: EP/R512400/1); Wellcome/EPSRC Centre for Interventional and Surgical Sciences (WEISS) (203145Z/16/Z); the NICEDROPS project supported by the European Research Council (ERC) under the European Union's Horizon 2020 research and innovation programme under grant agreement no. 714712; and Azkonobel and EPSRC for studentship for F.L.H. through the M³S Doctoral Training Centre (Grant EP/G036675).

References

- (1) Zhi, J.; Zhang, L. Z. Durable Superhydrophobic Surface with Highly Antireflective and Self-Cleaning Properties for the Glass Covers of Solar Cells. *Appl. Surf. Sci.* **2018**, *454* (May), 239–248. <https://doi.org/10.1016/j.apsusc.2018.05.139>.
- (2) Wu, Y.; Shen, Y.; Tao, J.; He, Z.; Xie, Y.; Chen, H.; Jin, M.; Hou, W. Facile Spraying Fabrication of Highly Flexible and Mechanically Robust Superhydrophobic F-SiO₂@PDMS Coatings for Self-Cleaning and Drag-Reduction Applications. *New J. Chem.* **2018**, *42* (22), 18208–18216. <https://doi.org/10.1039/C8NJ04275F>.
- (3) Ruan, M.; Zhan, Y.; Wu, Y.; Wang, X.; Li, W.; Chen, Y.; Wei, M.; Wang, X.; Deng, X. Preparation of PTFE/PDMS Superhydrophobic Coating and Its Anti-Icing

- Performance. *RSC Adv.* **2017**, 7 (66), 41339–41344.
<https://doi.org/10.1039/c7ra05264b>.
- (4) Grizen, M.; Maitra, T.; Bradley, J. P.; Tiwari, M. K. Nanotextured Aluminum-Based Surfaces with Icephobic Properties. *Heat Transf. Eng.* **2019**, 1–10.
<https://doi.org/10.1080/01457632.2019.1640461>.
- (5) Liu, Y.; Gu, H.; Jia, Y.; Liu, J.; Zhang, H.; Wang, R.; Zhang, B.; Zhang, H.; Zhang, Q. Design and Preparation of Biomimetic Polydimethylsiloxane (PDMS) Films with Superhydrophobic, Self-Healing and Drag Reduction Properties via Replication of Shark Skin and SI-ATRP. *Chem. Eng. J.* **2019**, 356, 318–328.
<https://doi.org/10.1016/j.cej.2018.09.022>.
- (6) Das, S.; Kumar, S.; Samal, S. K.; Mohanty, S.; Nayak, S. K. A Review on Superhydrophobic Polymer Nanocoatings: Recent Development and Applications. *Industrial and Engineering Chemistry Research.* **2018**, pp 2727–2745.
<https://doi.org/10.1021/acs.iecr.7b04887>.
- (7) Wenzel, R. N. Resistance of Solid Surface to Wetting by Water. *Industrial and Engineering Chemistry.* **1936**, pp 988–994.
- (8) Cassie, A. B. D.; Baxter, S. Wettability of Porous Surfaces. *Trans. Faraday Soc.* **1944**, 40, 546. <https://doi.org/10.1039/tf9444000546>.
- (9) Deng, Y.; Mager, D.; Bai, Y.; Zhou, T.; Liu, Z.; Wen, L.; Wu, Y.; Korvink, J. G. Inversely Designed Micro-Textures for Robust Cassie–Baxter Mode of Super-Hydrophobicity. *Comput. Methods Appl. Mech. Eng.* **2018**, 341, 113–132.
<https://doi.org/10.1016/j.cma.2018.06.034>.

- (10) Quéré, D. Wetting and Roughness. *Annu. Rev. Mater. Res.* **2008**, 38 (1), 71–99. <https://doi.org/10.1146/annurev.matsci.38.060407.132434>.
- (11) Shi, Z.; Zhang, Y.; Liu, M.; Hanaor, D. A. H.; Gan, Y. Dynamic Contact Angle Hysteresis in Liquid Bridges. *Colloids Surfaces A Physicochem. Eng. Asp.* **2018**, 555, 365–371. <https://doi.org/10.1016/j.colsurfa.2018.07.004>.
- (12) He, Z.; Ma, M.; Lan, X.; Chen, F.; Wang, K.; Deng, H.; Zhang, Q.; Fu, Q. Fabrication of a Transparent Superamphiphobic Coating with Improved Stability. *Soft Matter* **2011**, 7 (14), 6435–6443. <https://doi.org/10.1039/c1sm05574g>.
- (13) Brassard, J.-D.; Sarkar, D. K.; Perron, J. Fluorine Based Superhydrophobic Coatings. *Appl. Sci.* **2012**, 2 (4), 453–464. <https://doi.org/10.3390/app2020453>.
- (14) Pan, S.; Guo, R.; Björnmalm, M.; Richardson, J. J.; Li, L.; Peng, C.; Bertleff-Zieschang, N.; Xu, W.; Jiang, J.; Caruso, F. Coatings Super-Repellent to Ultralow Surface Tension Liquids. *Nat. Mater.* **2018**, 17 (11), 1040–1047. <https://doi.org/10.1038/s41563-018-0178-2>.
- (15) Liu, J.; Janjua, Z.; Roe, M.; Xu, F.; Turnbull, B.; Choi, K.-S.; Hou, X. Super-Hydrophobic/Icephobic Coatings Based on Silica Nanoparticles Modified by Self-Assembled Monolayers. *Nanomaterials* **2016**, 6 (12), 232. <https://doi.org/10.3390/nano6120232>.
- (16) Dalvi, V. H.; Rosky, P. J. Molecular Origins of Fluorocarbon Hydrophobicity. *Proc. Natl. Acad. Sci.* **2010**, 107 (31), 13603–13607. <https://doi.org/10.1073/pnas.0915169107>.

- (17) Nørgaard, A. W.; Hansen, J. S.; Sørli, J. B.; Levin, M.; Wolkoff, P.; Nielsen, G. D.; Larsen, S. T. Pulmonary Toxicity of Perfluorinated Silane-Based Nanofilm Spray Products: Solvent Dependency. *Toxicol. Sci.* **2014**, *137* (1), 179–188. <https://doi.org/10.1093/toxsci/kft225>.
- (18) Wang, Z.; Cousins, I. T.; Scheringer, M.; Hungerbuehler, K. Hazard Assessment of Fluorinated Alternatives to Long-Chain Perfluoroalkyl Acids (PFAAs) and Their Precursors: Status Quo, Ongoing Challenges and Possible Solutions. *Environ. Int.* **2015**, *75*, 172–179. <https://doi.org/10.1016/j.envint.2014.11.013>.
- (19) Blum, A.; Soehl, A. *Highly Fluorinated Chemicals (PFASs): Do the Benefits Justify the Harm?*; **2016**.
- (20) Yu, X.; Nishimura, F.; Hidaka, T. Enhanced Generation of Perfluoroalkyl Carboxylic Acids (PFCAs) from Fluorotelomer Alcohols (FTOHs) via Ammonia-Oxidation Process. *Chemosphere* **2018**, *198*, 311–319. <https://doi.org/10.1016/j.chemosphere.2018.01.132>.
- (21) Eklundh, T.; Supervisor, O.; Eriksson, U.; Kärrman, A. *Analytical Method Development of Fluorinated Silanes Using Mass Spectrometry*; **2018**.
- (22) Lee, E.; Lee, K. H. Facile Fabrication of Superhydrophobic Surfaces with Hierarchical Structures. *Sci. Rep.* **2018**, *8* (1), 4101. <https://doi.org/10.1038/s41598-018-22501-8>.
- (23) Zhang, P.; Dong, S.; Li, B.; Wei, X.; Zhang, J. Durable and Fluorine-Free Superhydrophobic Coatings from Palygorskite-Rich Spent Bleaching Earth. *Appl. Clay Sci.* **2018**, *157*, 237–247. <https://doi.org/10.1016/j.clay.2018.02.018>.

- (24) Khan, M. Z.; Baheti, V.; Militky, J.; Ali, A.; Vikova, M. Superhydrophobicity, UV Protection and Oil/Water Separation Properties of Fly Ash/Trimethoxy(Octadecyl)Silane Coated Cotton Fabrics. *Carbohydr. Polym.* **2018**, *202*, 571–580. <https://doi.org/10.1016/j.carbpol.2018.08.145>.
- (25) Heale, F. L.; Page, K.; Wixey, J. S.; Taylor, P.; Parkin, I. P.; Carmalt, C. J. Inexpensive and Non-Toxic Water Repellent Coatings Comprising SiO₂ Nanoparticles and Long Chain Fatty Acids. *RSC Adv.* **2018**, *8* (48), 27064–27072. <https://doi.org/10.1039/c8ra04707c>.
- (26) Peng, C.; Chen, Z.; Tiwari, M. K. All-Organic Superhydrophobic Coatings with Mechanochemical Robustness and Liquid Impalement Resistance. *Nat. Mater.* **2018**, *17* (4), 355–360. <https://doi.org/10.1038/s41563-018-0044-2>.
- (27) Tiwari, M. K.; Bayer, I. S.; Jursich, G. M.; Schutzius, T. M.; Megaridis, C. M. Highly Liquid-Repellent, Large-Area, Nanostructured Poly(Vinylidene Fluoride)/Poly(Ethyl 2-Cyanoacrylate) Composite Coatings: Particle Filler Effects. *ACS Appl. Mater. Interfaces* **2010**, *2* (4), 1114–1119. <https://doi.org/10.1021/am900894n>.
- (28) Narayan, R.; Nayak, U. Y.; Raichur, A. M.; Garg, S. Mesoporous Silica Nanoparticles: A Comprehensive Review on Synthesis and Recent Advances. *Pharmaceutics* **2018**, *10* (3), 1–49. <https://doi.org/10.3390/pharmaceutics10030118>.
- (29) Sun, B.; Zhou, G.; Zhang, H. Synthesis, Functionalization, and Applications of Morphology-Controllable Silica-Based Nanostructures: A Review. *Prog. Solid*

State Chem. **2016**, *44* (1), 1–19.
<https://doi.org/10.1016/j.progsolidstchem.2016.01.001>.

- (30) Wu, S.-H.; Mou, C.-Y.; Lin, H.-P. Synthesis of Mesoporous Silica Nanoparticles. *Chem. Soc. Rev* **2013**, *42* (42), 3649–4258.
- (31) Han, L.; Zhou, Y.; He, T.; Song, G.; Wu, F.; Jiang, F.; Hu, J. One-Pot Morphology-Controlled Synthesis of Various Shaped Mesoporous Silica Nanoparticles. *J. Mater. Sci.* **2013**, *48* (17), 5718–5726. <https://doi.org/10.1007/s10853-013-7501-8>.
- (32) Chantarak, S.; Chang, J.; Suwanboon, S.; Riyajan, S. One-Pot Synthesis of Ultrahydrophobic Mesoporous Silica Nanoparticles. *Mater. Res. Express* **2018**, *5* (9), 95030. <https://doi.org/10.1088/2053-1591/aad897>.
- (33) Zhi, D.; Wang, H.; Jiang, D.; Parkin, I. P.; Zhang, X. Reactive Silica Nanoparticles Turn Epoxy Coating from Hydrophilic to Super-Robust Superhydrophobic. *RSC Adv.* **2019**, *9* (22), 12547–12554. <https://doi.org/10.1039/c8ra10046b>.
- (34) Nguyen-tri, P.; Nguyen, T. A.; Carriere, P.; Xuan, C. N. Nanocomposite Coatings : Preparation , Characterization , Properties , and Applications. *Int. J. Corros.* **2018**, *2018*, 19.
- (35) Martin, S.; Bhushan, B. Transparent, Wear-Resistant, Superhydrophobic and Superoleophobic Poly(Dimethylsiloxane) (PDMS) Surfaces. *J. Colloid Interface Sci.* **2017**, *488*, 118–126. <https://doi.org/10.1016/j.jcis.2016.10.094>.
- (36) Zhao, X.; Li, Y.; Li, B.; Hu, T.; Yang, Y.; Li, L.; Zhang, J. Environmentally Benign

- and Durable Superhydrophobic Coatings Based on SiO₂ Nanoparticles and Silanes. *J. Colloid Interface Sci.* **2019**, *542*, 8–14. <https://doi.org/10.1016/j.jcis.2019.01.115>.
- (37) Gong, X.; He, S. Highly Durable Superhydrophobic Polydimethylsiloxane/Silica Nanocomposite Surfaces with Good Self-Cleaning Ability. *ACS Omega* **2020**, *5* (8), 4100–4108. <https://doi.org/10.1021/acsomega.9b03775>.
- (38) Gurav, A. B.; Xu, Q.; Latthe, S. S.; Vhatkar, R. S.; Liu, S.; Yoon, H.; Yoon, S. S. Superhydrophobic Coatings Prepared from Methyl-Modified Silica Particles Using Simple Dip-Coating Method. *Ceram. Int.* **2015**, *41* (2), 3017–3023. <https://doi.org/10.1016/j.ceramint.2014.10.137>.
- (39) Shang, Q.; Zhou, Y. Fabrication of Transparent Superhydrophobic Porous Silica Coating for Self-Cleaning and Anti-Fogging. *Ceram. Int.* **2016**, *42* (7), 8706–8712. <https://doi.org/10.1016/j.ceramint.2016.02.105>.
- (40) Vo, N. T.; Patra, A. K.; Kim, D. Pore Size and Concentration Effect of Mesoporous Silica Nanoparticles on the Coefficient of Thermal Expansion and Optical Transparency of Poly(Ether Sulfone) Films. *Phys. Chem. Chem. Phys.* **2017**, *19* (3), 1937–1944. <https://doi.org/10.1039/c6cp07545b>.
- (41) Xu, L.; Karunakaran, R. G.; Guo, J.; Yang, S. Transparent, Superhydrophobic Surfaces from One-Step Spin Coating of Hydrophobic Nanoparticles. *ACS Appl. Mater. Interfaces* **2012**, *4* (2), 1118–1125. <https://doi.org/10.1021/am201750h>.
- (42) Ejenstam, L.; Swerin, A.; Claesson, P. M. Toward Superhydrophobic Polydimethylsiloxane–Silica Particle Coatings. *J. Dispers. Sci. Technol.* **2016**, *37*

- (9), 1375–1383. <https://doi.org/10.1080/01932691.2015.1101610>.
- (43) Li, G.; Li, Z.; Lu, L.; Xue, L.; Deng, C. Fabrication and Wettable Investigation of Superhydrophobic Surface by Soft Lithography. *J. Wuhan Univ. Technol. Mater. Sci. Ed.* **2012**, *27* (1), 138–141. <https://doi.org/10.1007/s11595-012-0424-4>.
- (44) Sabbah, A.; Youssef, A.; Damman, P. Superhydrophobic Surfaces Created by Elastic Instability of PDMS. *Appl. Sci.* **2016**, *6* (5), 152. <https://doi.org/10.3390/app6050152>.
- (45) Dalod, A. R. M.; Grendal, O. G.; Blichfeld, A. B.; Furtula, V.; Pérez, J.; Henriksen, L.; Grande, T.; Einarsrud, M. A. Structure and Optical Properties of Titania-PDMS Hybrid Nanocomposites Prepared by in Situ Non-Aqueous Synthesis. *Nanomaterials* **2017**, *7* (12), 460. <https://doi.org/10.3390/nano7120460>.
- (46) Lu, Q. Synthesis of PDMS-Metal Oxide Hybrid Nanocomposites Using an in Situ Sol-Gel Route, Michigan Technological University, **2013**.
- (47) Crick, C. R.; Bear, J. C.; Kafizas, A.; Parkin, I. P. Superhydrophobic Photocatalytic Surfaces through Direct Incorporation of Titania Nanoparticles into a Polymer Matrix by Aerosol Assisted Chemical Vapor Deposition. *Adv. Mater.* **2012**, *24* (26), 3505–3508. <https://doi.org/10.1002/adma.201201239>.
- (48) Ali, H. M.; Qasim, M. A.; Malik, S.; Murtaza, G. *Techniques for the Fabrication of Super-Hydrophobic Surfaces and Their Heat Transfer Applications*; Konstantin Volkov, Ed.; InTech: London, **2018**. <https://doi.org/10.5772/intechopen.71737>.
- (49) Wang, Y.; Zhu, Y.; Zhang, C.; Li, J.; Guan, Z. Transparent, Superhydrophobic

- Surface with Varied Surface Tension Responsiveness in Wettability Based on Tunable Porous Silica Structure for Gauging Liquid Surface Tension. *ACS Appl. Mater. Interfaces* **2017**, *9* (4), 4142–4150. <https://doi.org/10.1021/acsami.6b12779>.
- (50) Long, M.; Peng, S.; Deng, W.; Yang, X.; Miao, K.; Wen, N.; Miao, X.; Deng, W. Robust and Thermal-Healing Superhydrophobic Surfaces by Spin-Coating of Polydimethylsiloxane. *J. Colloid Interface Sci.* **2017**, *508*, 18–27. <https://doi.org/10.1016/j.jcis.2017.08.027>.
- (51) Marchand, P.; Hassan, I. A.; Parkin, I. P.; Carmalt, C. J. Aerosol-Assisted Delivery of Precursors for Chemical Vapour Deposition: Expanding the Scope of CVD for Materials Fabrication. *Dalt. Trans.* **2013**, *42* (26), 9406. <https://doi.org/10.1039/c3dt50607j>.
- (52) Crick, C. R.; Parkin, I. P. Superhydrophobic Silica Films on Glass Formed by Hydrolysis of an Acidic Aerosol of Tetraethylorthosilicate. *J. Mater. Chem.* **2011**, *21* (25), 9362–9366. <https://doi.org/10.1039/c1jm10825e>.
- (53) Ponja, S. D.; Parkin, I. P.; Carmalt, C. J. Synthesis and Material Characterization of Amorphous and Crystalline (α -) Al₂O₃: Via Aerosol Assisted Chemical Vapour Deposition. *RSC Adv.* **2016**, *6* (105), 102956–102960. <https://doi.org/10.1039/c6ra24018f>.
- (54) Powell, M. J.; Potter, D. B.; Wilson, R. L.; Darr, J. A.; Parkin, I. P.; Carmalt, C. J. Scaling Aerosol Assisted Chemical Vapour Deposition: Exploring the Relationship between Growth Rate and Film Properties. *Mater. Des.* **2017**, *129*, 116–124.

<https://doi.org/10.1016/j.matdes.2017.05.017>.

- (55) Chadwick, N.; Sathasivam, S.; Kafizas, A.; Bawaked, S. M.; Obaid, A. Y.; Al-Thabaiti, S.; Basahel, S. N.; Parkin, I. P.; Carmalt, C. J. Combinatorial Aerosol Assisted Chemical Vapour Deposition of a Photocatalytic Mixed SnO₂/TiO₂ Thin Film. *J. Mater. Chem. A* **2014**, *2* (14), 5108–5116. <https://doi.org/10.1039/C4TA00545G>.
- (56) Chuah, Y. J.; Koh, Y. T.; Lim, K.; Menon, N. V.; Wu, Y.; Kang, Y. Simple Surface Engineering of Polydimethylsiloxane with Polydopamine for Stabilized Mesenchymal Stem Cell Adhesion and Multipotency. *Sci. Rep.* **2015**, *5* (December). <https://doi.org/10.1038/srep18162>.
- (57) Luechinger, M.; Prins, R.; Pirngruber, G. D. Functionalization of Silica Surfaces with Mixtures of 3-Aminopropyl and Methyl Groups. *Microporous Mesoporous Mater.* **2005**, *85* (1–2), 111–118. <https://doi.org/10.1016/j.micromeso.2005.05.031>.
- (58) Anbalagan, G.; Prabakaran, A. R.; Gunasekaran, S. Spectroscopic Characterization of Indian Standard Sand. *J. Appl. Spectrosc.* **2010**, *77* (1), 86–94. <https://doi.org/10.1007/s10812-010-9297-5>.
- (59) Trébosc, J.; Wiench, J. W.; Huh, S.; Lin, V. S. Y.; Pruski, M. Solid-State MMR Study of MCM-41-Type Mesoporous Silica Nanoparticles. *J. Am. Chem. Soc.* **2005**, *127* (9), 3057–3068. <https://doi.org/10.1021/ja043567e>.
- (60) Vo, N. T.; Patra, A. K.; Kim, D. Pore Size and Concentration Effect of Mesoporous Silica Nanoparticles on the Coefficient of Thermal Expansion and Optical

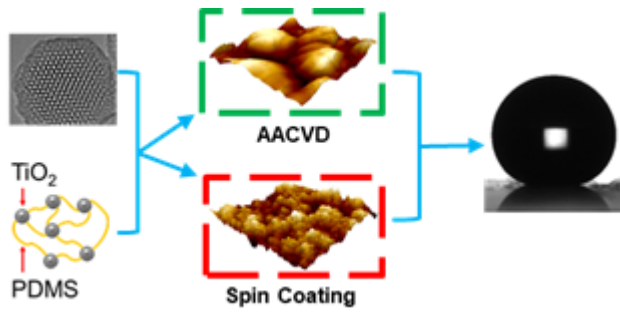
- Transparency of Poly(Ether Sulfone) Films. *Phys. Chem. Chem. Phys.* **2017**, *19* (3), 1937–1944. <https://doi.org/10.1039/c6cp07545b>.
- (61) Suzuki, N.; Zakaria, M. B.; Chiang, Y. D.; Wu, K. C. W.; Yamauchi, Y. Thermally Stable Polymer Composites with Improved Transparency by Using Colloidal Mesoporous Silica Nanoparticles as Inorganic Fillers. *Phys. Chem. Chem. Phys.* **2012**, *14* (20), 7427–7432. <https://doi.org/10.1039/c2cp40356k>.
- (62) Mehmood, A.; Ghafar, H.; Yaqoob, S.; Gohar, U. F.; Ahmad, B. Mesoporous Silica Nanoparticles: A Review. *J. Dev. Drugs* **2017**, *06* (02). <https://doi.org/10.4172/2329-6631.1000174>.
- (63) Liu, J.; Zong, G.; He, L.; Zhang, Y.; Liu, C.; Wang, L. Effects of Fumed and Mesoporous Silica Nanoparticles on the Properties of Sylgard 184 Polydimethylsiloxane. *Micromachines* **2015**, *6* (7), 855–864. <https://doi.org/10.3390/mi6070855>.
- (64) Tombesi, A.; Li, S.; Sathasivam, S.; Page, K.; Heale, F. L.; Pettinari, C.; Carmalt, C. J.; Parkin, I. P. Aerosol-Assisted Chemical Vapour Deposition of Transparent Superhydrophobic Film by Using Mixed Functional Alkoxysilanes. *Sci. Rep.* **2019**, *9* (1). <https://doi.org/10.1038/s41598-019-43386-1>.
- (65) Guo, X. J.; Xue, C. H.; Sathasivam, S.; Page, K.; He, G.; Guo, J.; Promdet, P.; Heale, F. L.; Carmalt, C. J.; Parkin, I. P. Fabrication of Robust Superhydrophobic Surfaces: Via Aerosol-Assisted CVD and Thermo-Triggered Healing of Superhydrophobicity by Recovery of Roughness Structures. *J. Mater. Chem. A* **2019**, *7* (29), 17604–17612. <https://doi.org/10.1039/c9ta03264a>.

- (66) Li, S.; Page, K.; Sathasivam, S.; Heale, F.; He, G.; Lu, Y.; Lai, Y.; Chen, G.; Carmalt, C. J.; Parkin, I. P. Efficiently Texturing Hierarchical Superhydrophobic Fluoride-Free Translucent Films by AACVD with Excellent Durability and Self-Cleaning Ability. *J. Mater. Chem. A* **2018**, *6* (36), 17633–17641. <https://doi.org/10.1039/c8ta05402a>.
- (67) Nyamukamba, P.; Okoh, O.; Mungondori, H.; Taziwa, R.; Zinya, S. *Synthetic Methods for Titanium Dioxide Nanoparticles: A Review*; Dongfang Yang, Ed.; ItechOpen: London, **2018**. <https://doi.org/10.5772/intechopen.70290>.
- (68) Lu, Y.; Sathasivam, S.; Song, J.; Crick, C. R.; Carmalt, C. J.; Parkin, I. P. Robust Self-Cleaning Surfaces That Function When Exposed to Either Air or Oil. *Science (80-.)*. **2015**, *347* (6226), 1132–1135. <https://doi.org/10.1126/science.aaa0946>.
- (69) Sebastian, D.; Yao, C. W.; Lian, I. Abrasion Resistance of Superhydrophobic Coatings on Aluminum Using PDMS/SiO₂. *Coatings* **2018**, *8* (11), 414. <https://doi.org/10.3390/COATINGS8110414>.
- (70) Wang, J.; Lu, Y.; Chu, Q.; Ma, C.; Cai, L.; Shen, Z.; Chen, H. Facile Construction of Superhydrophobic Surfaces by Coating Fluoroalkylsilane/Silica Composite on a Modified Hierarchical Structure of Wood. *Polymers (Basel)*. **2020**, *12* (4). <https://doi.org/10.3390/POLYM12040813>.
- (71) Zhuang, A.; Liao, R.; Dixon, S. C.; Lu, Y.; Sathasivam, S.; Parkin, I. P.; Carmalt, C. J. Transparent Superhydrophobic PTFE Films via One-Step Aerosol Assisted Chemical Vapor Deposition. *RSC Adv.* **2017**, *7* (47), 29275–29283. <https://doi.org/10.1039/c7ra04116k>.

- (72) Prasad, G.; Chakradhar, R. P. S.; Bera, P.; Prabu, A. A.; Anandan, C. Transparent Hydrophobic and Superhydrophobic Coatings Fabricated Using Polyamide 12–SiO₂ Nanocomposite. *Surf. Interface Anal.* **2017**, *49* (5), 427–433. <https://doi.org/10.1002/sia.6175>.
- (73) Janjua, Z.; Xu, F.; Choi, K.-S.; Turnbull, B.; Liu, J.; Hou, X.; Roe, M. Super-Hydrophobic/Icephobic Coatings Based on Silica Nanoparticles Modified by Self-Assembled Monolayers. *Nanomaterials* **2016**, *6* (12), 232. <https://doi.org/10.3390/nano6120232>.
- (74) Li, F.; Du, M.; Zheng, Z.; Song, Y.; Zheng, Q. A Facile, Multifunctional, Transparent, and Superhydrophobic Coating Based on a Nanoscale Porous Structure Spontaneously Assembled from Branched Silica Nanoparticles. *Adv. Mater. Interfaces* **2015**, *2* (13), 1500201. <https://doi.org/10.1002/admi.201500201>.
- (75) Xu, L.; He, J. Fabrication of Highly Transparent Superhydrophobic Coatings from Hollow Silica Nanoparticles. *Langmuir* **2012**, *28* (19), 7512–7518. <https://doi.org/10.1021/la301420p>.
- (76) Zou, X.; Tao, C.; Yang, K.; Yang, F.; Lv, H.; Yan, L.; Yan, H.; Li, Y.; Xie, Y.; Yuan, X.; et al. Rational Design and Fabrication of Highly Transparent, Flexible, and Thermally Stable Superhydrophobic Coatings from Raspberry-like Hollow Silica Nanoparticles. *Appl. Surf. Sci.* **2018**, *440*, 700–711. <https://doi.org/10.1016/j.apsusc.2018.01.159>.
- (77) Zhang, X.; Lan, P.; Lu, Y.; Li, J.; Xu, H.; Zhang, J.; Lee, Y.; Rhee, J. Y.; Choy, K. L.; Song, W. Multifunctional Antireflection Coatings Based on Novel Hollow Silica-

- Silica Nanocomposites. *ACS Appl. Mater. Interfaces* **2014**, 6 (3), 1415–1423.
<https://doi.org/10.1021/am405258d>.
- (78) Zhao, X.; Park, D. S.; Choi, J.; Park, S.; Soper, S. A.; Murphy, M. C. Robust, Transparent, Superhydrophobic Coatings Using Novel Hydrophobic/Hydrophilic Dual-Sized Silica Particles. *J. Colloid Interface Sci.* **2020**, 574, 347–354.
<https://doi.org/10.1016/j.jcis.2020.04.065>.
- (79) Deng, X.; Mammen, L.; Zhao, Y.; Lellig, P.; Müllen, K.; Li, C.; Butt, H. J.; Vollmer, D. Transparent, Thermally Stable and Mechanically Robust Superhydrophobic Surfaces Made from Porous Silica Capsules. *Adv. Mater.* **2011**, 23 (26), 2962–2965. <https://doi.org/10.1002/adma.201100410>.
- (80) Tombesi, A.; Li, S.; Sathasivam, S.; Page, K.; Heale, F. L.; Pettinari, C.; Carmalt, C. J.; Parkin, I. P. Aerosol-Assisted Chemical Vapour Deposition of Transparent Superhydrophobic Film by Using Mixed Functional Alkoxysilanes. *Sci. Rep.* **2019**, 9 (1). <https://doi.org/10.1038/s41598-019-43386-1>.
- (81) Bayer, I. S. On the Durability and Wear Resistance of Transparent Superhydrophobic Coatings. *Coatings* **2017**, 7 (1).
<https://doi.org/10.3390/coatings7010012>.
- (82) Zhang, Y.; Dong, B.; Wang, S.; Zhao, L.; Wan, L.; Wang, E. Mechanically Robust, Thermally Stable, Highly Transparent Superhydrophobic Coating with Low-Temperature Sol-Gel Process. *RSC Adv.* **2017**, 7 (75), 47357–47365.
<https://doi.org/10.1039/c7ra08578h>.
- (83) Mahadik, S. A.; Kavale, M. S.; Mukherjee, S. K.; Rao, A. V. Transparent

- Superhydrophobic Silica Coatings on Glass by Sol-Gel Method. *Appl. Surf. Sci.* **2010**, 257 (2), 333–339. <https://doi.org/10.1016/j.apsusc.2010.06.062>.
- (84) Luo, G. F.; Chen, W. H.; Liu, Y.; Zhang, J.; Cheng, S. X.; Zhuo, R. X.; Zhang, X. Z. Charge-Reversal Plug Gate Nanovalves on Peptide-Functionalized Mesoporous Silica Nanoparticles for Targeted Drug Delivery. *J. Mater. Chem. B* **2013**, 1 (41), 5723–5732. <https://doi.org/10.1039/c3tb20792g>.
- (85) Dalod, A.; Grendal, O.; Blichfeld, A.; Furtula, V.; Pérez, J.; Henriksen, L.; Grande, T.; Einarsrud, M.-A. Structure and Optical Properties of Titania-PDMS Hybrid Nanocomposites Prepared by In Situ Non-Aqueous Synthesis. *Nanomaterials* **2017**, 7 (12), 460. <https://doi.org/10.3390/nano7120460>.



For Table of Contents Only